## **OPEN ACCESS**



# Beyond Spectroscopy. II. Stellar Parameters for over 20 Million Stars in the Northern Sky from SAGES DR1 and Gaia DR3

Yang Huang<sup>1,2</sup>, Timothy C. Beers<sup>3</sup>, Haibo Yuan<sup>4</sup>, Ke-Feng Tan<sup>2</sup>, Wei Wang<sup>2</sup>, Jie Zheng<sup>2</sup>, Chun Li<sup>2</sup>, Young Sun Lee<sup>5</sup>, Hai-Ning Li<sup>2</sup>, Jing-Kun Zhao<sup>2</sup>, Xiang-Xiang Xue<sup>2</sup>, Yujuan Liu<sup>2</sup>, Huawei Zhang<sup>6,7</sup>, Xue-Ang Sun<sup>8</sup>, Ji Li<sup>8</sup>, Hong-Rui Gu<sup>2,1</sup>, Christian Wolf<sup>9,10</sup>, Christopher A. Onken<sup>9,10</sup>, Jifeng Liu<sup>2,1</sup>, Zhou Fan<sup>2,1</sup>, and Gang Zhao<sup>2,1</sup> School of Astronomy and Space Science, University of Chinese Academy of Sciences, Beijing 100049, People's Republic of China; hunagyang@ucas.ac.cn<sup>2</sup> Key Lab of Optical Astronomy, National Astronomical Observatories, Chinese Academy of Sciences, Beijing 100012, People's Republic of China; zfan@bao.ac.cn, gzhao@nao.ac.cn

3 Department of Physics and Astronomy and JINA Center for the Evolution of the Elements (JINA-CEE), University of Notre Dame, Notre Dame, IN 46556, USA

Department of Astronomy, Beijing Normal University, Beijing 100875, People's Republic of China

<sup>5</sup> Department of Astronomy and Space Science, Chungnam National University, Daejeon 34134, Republic of Korea Department of Astronomy, School of Physics, Peking University, Beijing 100871, People's Republic of China Kavli Institute for Astronomy and Astrophysics, Peking University, Beijing 100871, People's Republic of China <sup>8</sup> Department of Space Science and Astronomy, Hebei Normal University, Shijiazhuang 050024, People's Republic of China

Received 2023 March 22; revised 2023 July 3; accepted 2023 July 9; published 2023 October 30

#### Abstract

We present precise photometric estimates of stellar parameters, including effective temperature, metallicity, luminosity classification, distance, and stellar age, for nearly 26 million stars using the methodology developed in the first paper of this series, based on the stellar colors from the Stellar Abundances and Galactic Evolution Survey (SAGES) Data Release 1 and Gaia Early Data Release 3. The optimal design of stellar-parameter sensitive uv filters by SAGES has enabled us to determine photometric-metallicity estimates down to -3.5, similar to our previous results with the SkyMapper Southern Survey (SMSS), yielding a large sample of over five million metal-poor  $([Fe/H] \le -1.0)$  stars and nearly one million very metal-poor  $([Fe/H] \le -2.0)$  stars. The typical precision is around 0.1 dex for both dwarf and giant stars with [Fe/H] > -1.0, and 0.15-0.25/0.3-0.4 dex for dwarf/giant stars with [Fe/H] < -1.0. Using the precise parallax measurements and stellar colors from Gaia, effective temperature, luminosity classification, distance, and stellar age are further derived for our sample stars. This huge data set in the Northern sky from SAGES, together with similar data in the Southern sky from SMSS, will greatly advance our understanding of the Milky Way, in particular its formation and evolution.

Unified Astronomy Thesaurus concepts: Fundamental parameters of stars (555); Ultraviolet surveys (1742); Galaxy abundances (574); Milky Way Galaxy (1054)

#### 1. Introduction

Estimates of stellar parameters, in particular the metallicity, of a large, complete sample of stars is of vital importance to understand the formation and evolution of the Milky Way. In the past decades, massive progress has been achieved by largescale spectroscopic surveys, such as the HK Survey (Beers et al. 1985, 1992), the Hamburg/ESO Survey (Christlieb 2003) the Sloan Digital Sky Survey (SDSS; York et al. 2000), the Radial Velocity Experiment (RAVE; Steinmetz et al. 2006), the Large Sky Area Multi-Object Fiber Spectroscopic Telescope (LAMOST; Deng et al. 2012; Liu et al. 2014), the Galactic Archaeology with HERMES project (GALAH; De Silva et al. 2015), and the Apache Point Observatory Galactic Evolution Experiment (APOGEE; Majewski et al. 2017). However, the total number of observed targets collected from all those surveys is no greater than about 10 million, less than 1/10,000of the estimated total numbers of Milky Way stars. This undersampling, together with the complex target-selection

Original content from this work may be used under the terms of the Creative Commons Attribution 4.0 licence. Any further distribution of this work must maintain attribution to the author(s) and the title of the work, journal citation and DOI.

strategies, makes it extremely difficult to understand the full assembly history of our Galaxy.

In the first paper of this series (Huang et al. 2022, hereafter H22), we proposed to alleviate this issue of current spectroscopic surveys by deriving stellar parameters for a huge number of stars using narrow/medium-bandwidth photometric surveys (see Table 1 of H22 for a summary). As a pioneering experiment, H22 present measurements of stellar parameters, including metallicity, luminosity classification, effective temperature, distance, and stellar age, for over 24 million stars, based on the stellar colors from the SkyMapper Southern Survey (SMSS; Wolf et al. 2018; Onken et al. 2019) and Gaia (Gaia Collaboration et al. 2021), as well as the parallax measurements from Gaia. This huge data set has already been applied to a number of Galactic studies, including searching for metal-poor stars (Zepeda et al. 2022), discovery of ancient halo substructures (Shank et al. 2022a, 2022b; Yuan et al. 2022), and understanding the disk/halo formation history (J. Hong et al. 2023, in preparation). Its contribution to this field is just beginning to be explored.

In this paper, we present a second pioneering experiment in the Northern sky, using the data from the first data release of the Stellar Abundance and Galactic Evolution Survey Data Release 1 (SAGES DR1; Fan et al. 2023) and Gaia Early Data

Research School of Astronomy and Astrophysics, Australian National University, Canberra, ACT 2611, Australia <sup>10</sup> Centre for Gravitational Astrophysics, Research Schools of Physics, and Astronomy and Astrophysics, Australian National University, Canberra, ACT 2611, Australia

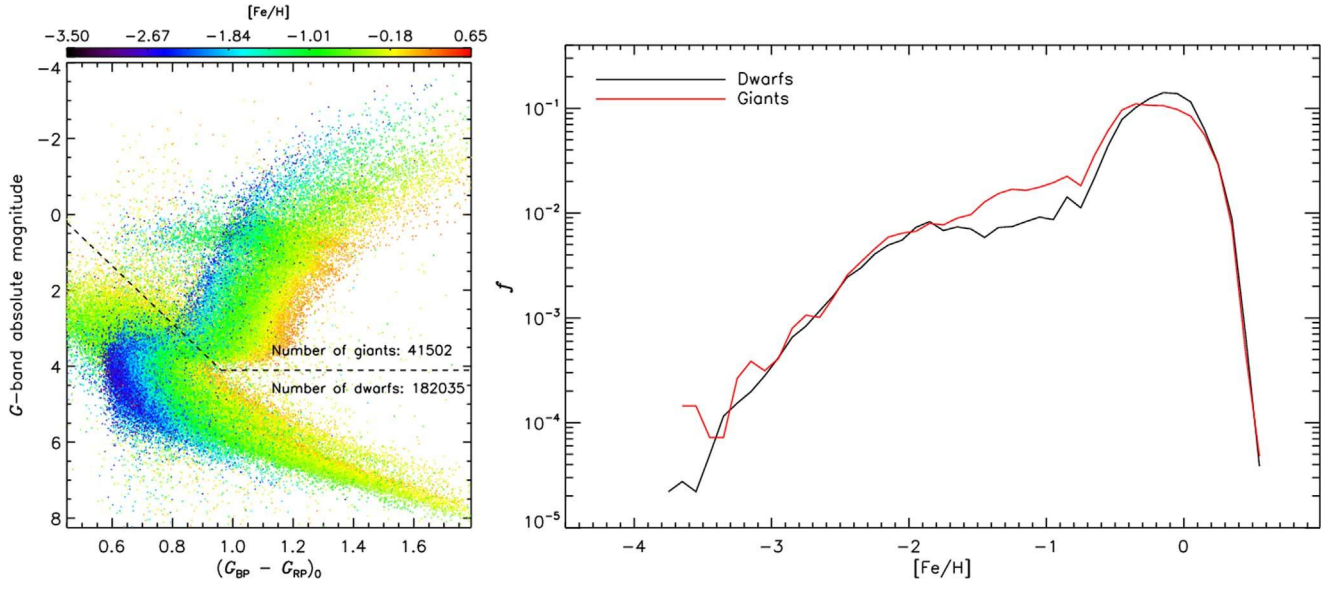


Figure 1. Left panel: Hertzsprung–Russell (H-R) diagram,  $M_{G_0}$  vs.  $(G_{BP} - G_{RP})_0$ , of the stars in the training set defined in Section 3.1, color coded by [Fe/H] as shown in the color bar at the top. The dashed lines represent the empirical cuts  $M_{G_0} = -3.20 + 7.60 \cdot (G_{BP} - G_{RP})_0$  or  $M_{G_0} = 4.1$ , used to separate dwarf and giant stars. Right panel: metallicity ([Fe/H]) distributions of dwarf (black line) and giant (red line) stars in the training sample.

 Table 1

 Fit Coefficients for Metallicity Estimates for Dwarf and Giant Stars

Coeff.	Dwarf Stars		Giant Stars	
	$(u-G_{\rm BP})_0^{\rm a}$	$(v-G_{\rm BP})_0^{\ \ b}$	$(u-G_{\rm BP})_0^{\rm a}$	$(v-G_{\rm BP})_0^{{\rm b}}$
$a_{0,0}$	3.084320	0.694670	3.603653	0.372304
$a_{0,1}$	-0.587864	-0.067923	-1.418031	-0.185474
$a_{0,2}$	0.016439	0.097577	0.000912	0.087328
$a_{0,3}$	0.022031	0.008902	0.026515	-0.001555
$a_{1,0}$	-8.246335	-2.465311	-9.413692	-1.103181
$a_{1,1}$	1.795641	0.589683	3.089203	0.830962
$a_{1,2}$	0.160856	-0.043831	0.178593	-0.059142
$a_{2,0}$	10.296704	4.577793	10.752706	2.737885
$a_{2,2}$	-0.676539	-0.262572	-1.183446	-0.370985
$a_{3,0}$	-3.201283	-1.498611	-2.972827	-0.727921

#### Notes.

Release 3 (EDR3; Gaia Collaboration et al. 2021). SAGES is an optical multiband (u, v, g, r, i, DDO -51,  $H\alpha_{\rm wide}$ ,  $H\alpha_{\rm narrow}$ ) large-scale photometric survey, aiming to cover 12,000 deg $^2$  of the Northern sky with  $\delta > -5^{\circ}$  down to a  $5\sigma$  depth of 21.5 in the u band (Zheng et al. 2018). The u-band filter is the same as in the Strömgren system (Strömgren 1956), and the v band is optimized to provide reliable metallicity measurements by shifting the central wavelength of the SkyMapper v (Bessell et al. 2011) to longer wavelengths, by about 100 Å, to reduce the effect of molecular bands of carbon and nitrogen on the metallicity estimates.

The special design of the *uv* filters (especially the *v* band) provides photometric sensitivity to stellar surface gravity and metallicity that are well demonstrated by numerous previous efforts with similar filter systems (e.g., Nordström et al. 2004;

Starkenburg et al. 2017; Casagrande et al. 2019; Huang et al. 2019; Chiti et al. 2021; H22). The gri filters are SDSS-like, which can be used to estimate the stellar effective temperature. The combination of  $H\alpha$  and other filters can be used to estimate the values of reddening. Similar to our effort with SMSS (H22), here we present stellar-parameter estimates for about 26 million stars using the uv-band data released in SAGES DR1, along with the photometric and parallax information provided by Gaia EDR3 (Gaia Collaboration et al. 2021).

This paper is structured as follows. In Section 2, we introduce the data adopted in the current work. In Section 3, photometric-metallicity estimates from the stellar colors of SAGES DR1 and Gaia EDR3 are described, along with various checks on the photometric measurements. The determinations of effective temperature,  $T_{\rm eff}$ , distance, and age are presented in Section 4. Radial-velocity measurements collected from previous spectroscopic surveys and the final sample are described in Section 5. We present a summary in Section 6.

## 2. Data

In the present work, the SAGES DR1 (Fan et al. 2023) data set is adopted. SAGES DR1 has released a total of about 100 million sources extracted from 36,092 accepted frames in the uv bands collected by the 90 inch (2.3 m) Bok Telescope at Kitt Peak National Observatory in Arizona. DR1 covers about half of the Northern Hemisphere (9960  $\deg^2$ ), about 90% of the planned area. The median completeness is about 20.4 and 20.3 for the u and v band, respectively. This is one of the deepest near-ultraviolet large-scale photometric survey with a  $5\sigma$  depth close to 21.5 in the u band. Compared to other near-ultraviolet deep photometric surveys, e.g., the SDSS (York et al. 2000) and the South Galactic Cap u-band Sky Survey (Zhou et al. 2016), SAGES has the advantage of using the two mediumbandwidth uv filters, which are optimized for estimates of stellar parameters.

In addition to the uv-band data provided by SAGES DR1, the optical bands of G,  $G_{\rm BP}$ , and  $G_{\rm RP}$ , as well as astrometric information, are adopted from the Gaia EDR3 (Gaia

<sup>&</sup>lt;sup>a</sup>  $(u - G_{\rm BP})_0 = a_{0.0} + a_{0.1}y + a_{0.2}y^2 + a_{0.3}y^3 + a_{1.0}x + a_{1.1}xy + a_{1.2}xy^2 + a_{2.0}x^2 + a_{2.1}x^2y + a_{3.0}x^3$ , where x and y represent  $(G_{\rm BP} - G_{\rm RP})_0$  and [Fe/H], respectively.

<sup>&</sup>lt;sup>b</sup>  $(v - G_{BP})_0 = a_{0,0} + a_{0,1}y + a_{0,2}y^2 + a_{0,3}y^3 + a_{1,0}x + a_{1,1}xy + a_{1,2}xy^2 + a_{2,0}x^2 + a_{2,1}x^2y + a_{3,0}x^3$ , where x and y represent  $(G_{BP} - G_{RP})_0$  and [Fe/H], respectively.

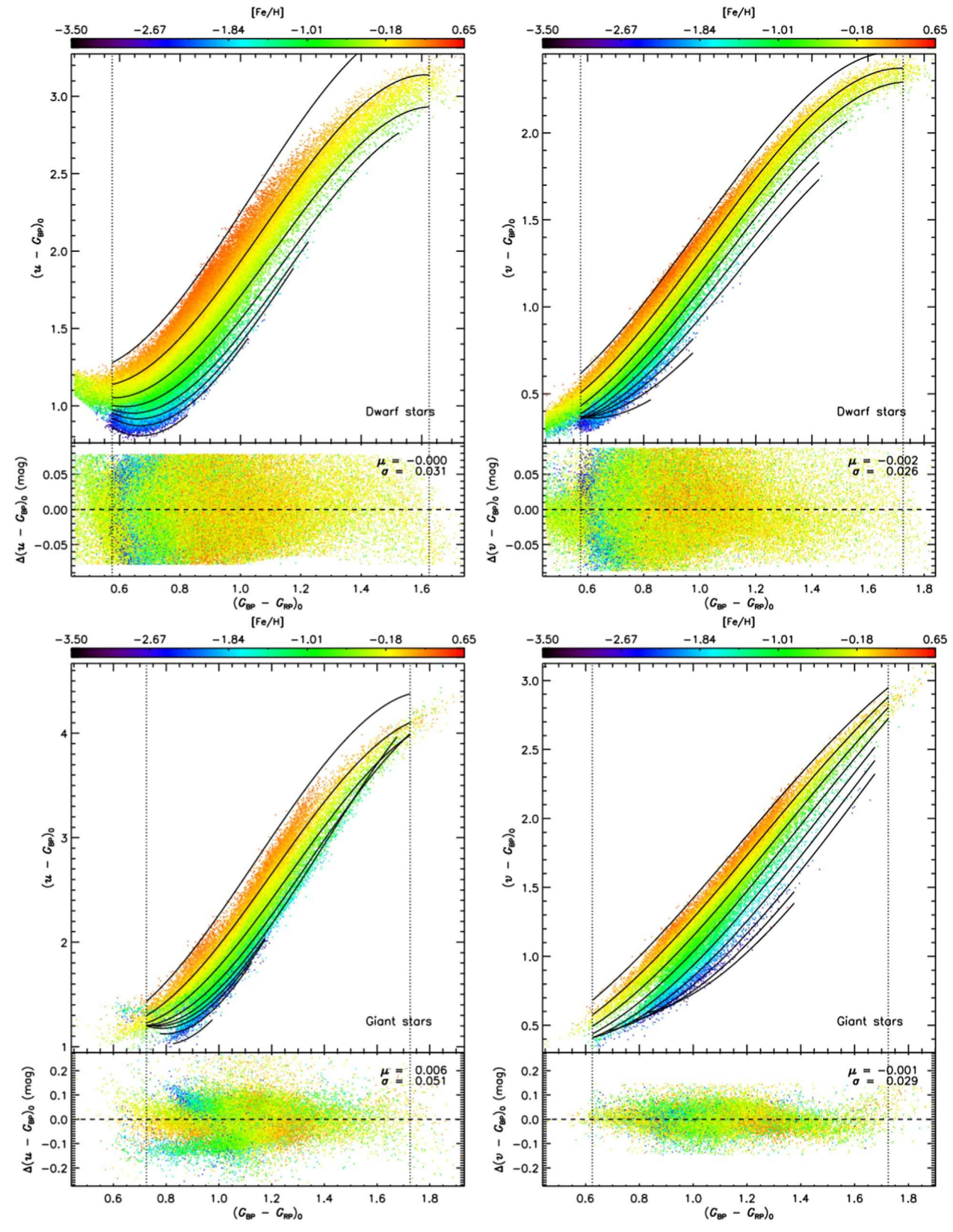


Figure 2. Top: metallicity-dependent stellar loci of training-set dwarf stars in the plane of  $(u - G_{BP})_0$  vs.  $(G_{BP} - G_{RP})_0$  (left panel) and  $(v - G_{BP})_0$  vs.  $(G_{BP} - G_{RP})_0$  (right panel), color coded by [Fe/H] as shown in the top color bars. The black lines represent our best fits for [Fe/H] with values ranging from +0.5 (top) to -3.5 (bottom) in steps of 0.5 dex, as described by Equation (1). The dashed lines mark the color region in  $(G_{BP} - G_{RP})_0$  for which the data points yield robust fits. The lower part of each panel shows the fit residual, as a function of color  $(G_{BP} - G_{RP})_0$ , with the values of median and standard deviation of the residual marked in the top-right corner. Bottom: similar to the top panels, but for training-set giant stars.

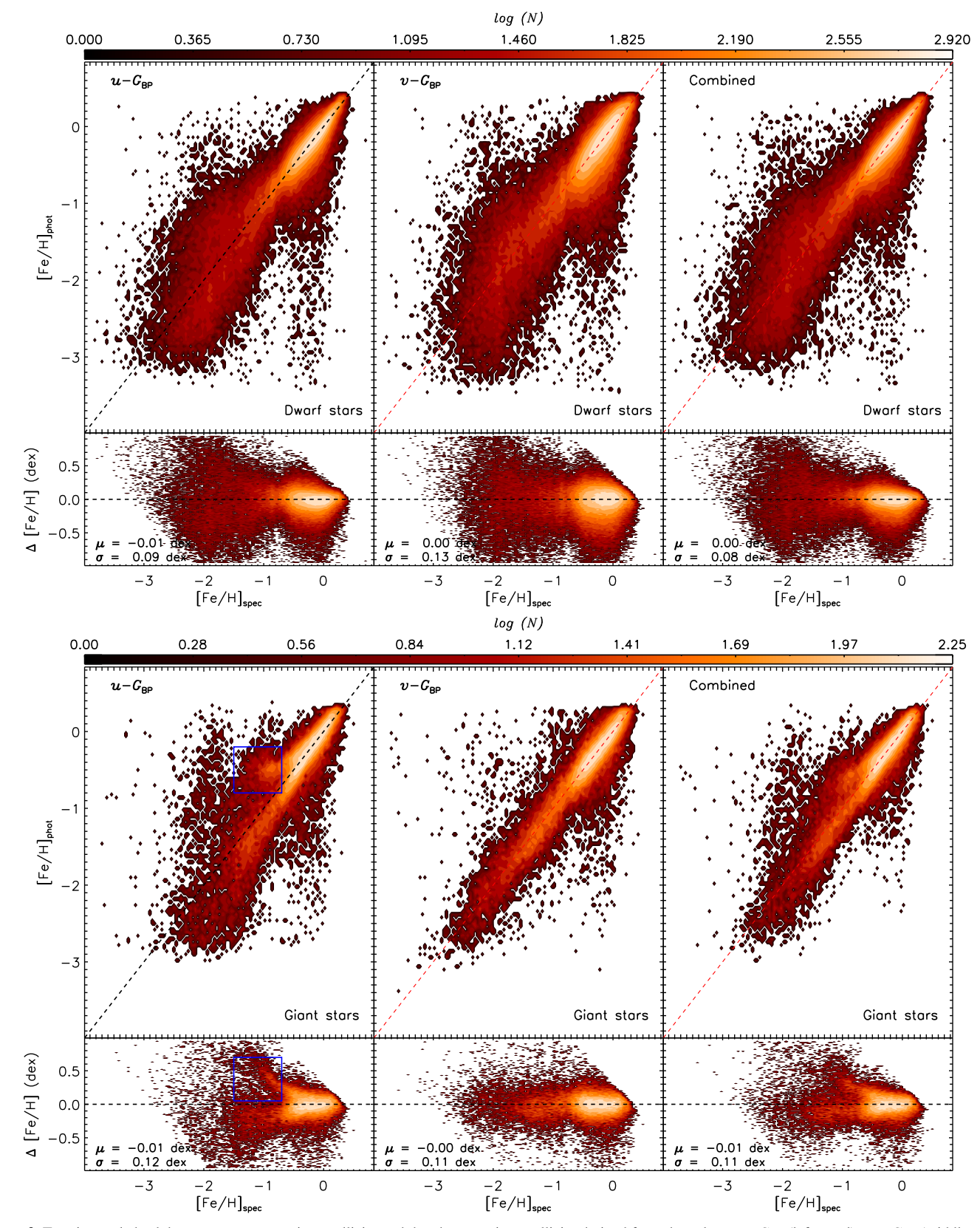
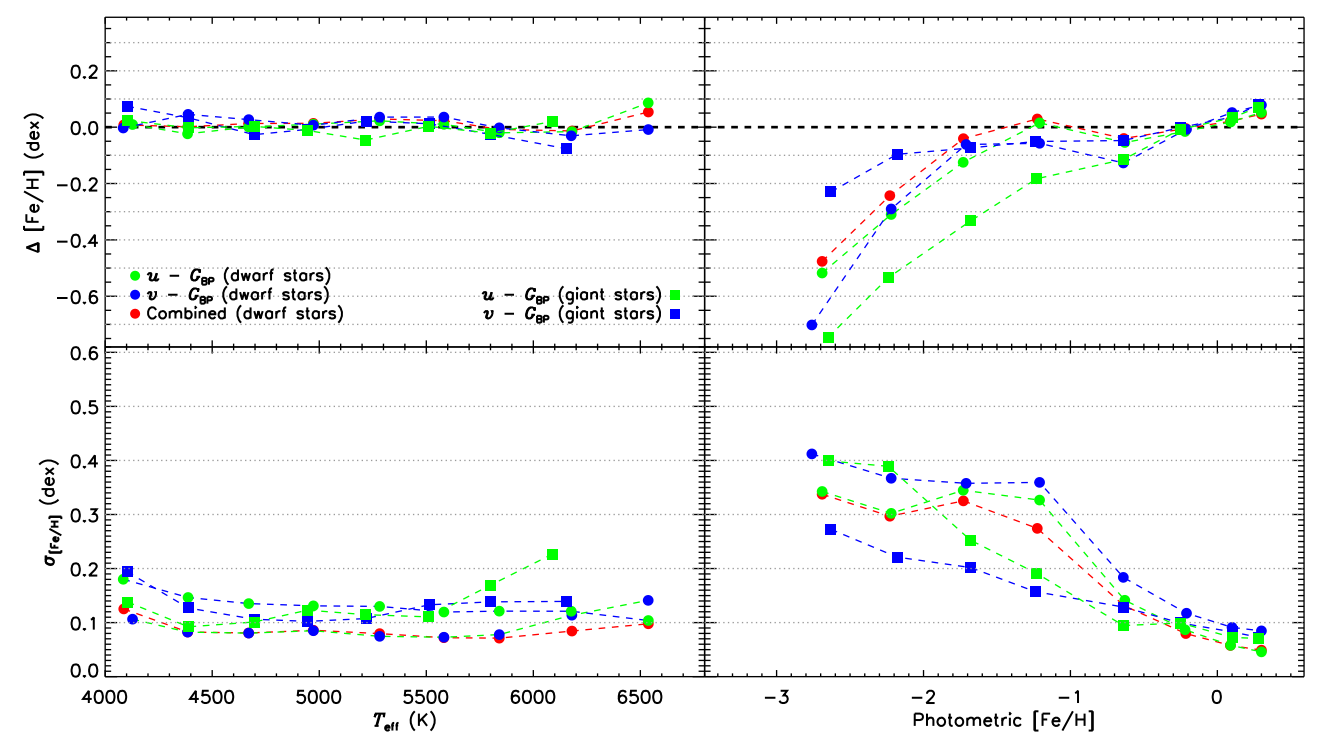
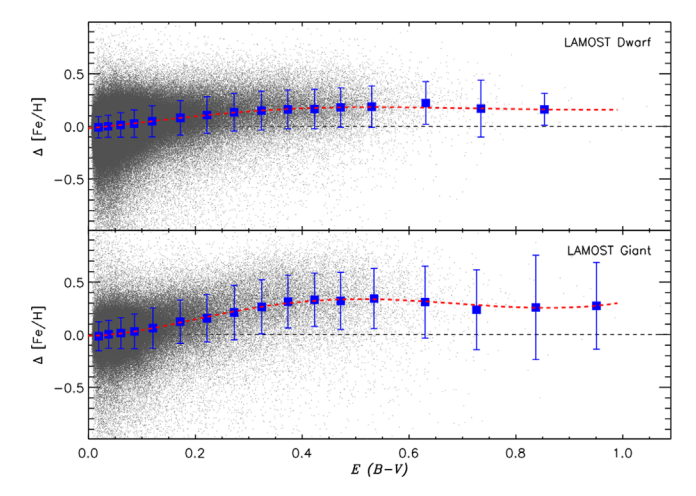


Figure 3. Top: internal check between spectroscopic metallicity and the photometric metallicity derived from the colors  $u - G_{\rm BP}$  (left panel),  $v - G_{\rm BP}$  (middle panel), and the combination of the two colors (right panel), using a maximum-likelihood approach (see Section 3.2) for the training-set dwarf stars. The metallicity difference (photometric minus spectroscopic), as a function of the spectroscopic metallicity, is shown in the lower part of each panel, with the median and standard deviation of the difference marked in the bottom-left corner. In each panel, a color-coded contour of the stellar number density on a logarithmic scale is shown. Bottom: similar to the top panels, but for the training-set giant stars. In the left panel, a region of stars marked by the blue box with large deviations from the spectroscopic estimates are mainly from warm, low-gravity blue giants, e.g., the blue horizontal-branch stars.



**Figure 4.** Median offsets (top panels) and standard deviations (bottom panels) of the metallicity differences (photometric minus spectroscopic), as a function of effective temperature (left panels) and photometric [Fe/H] (right panels), as calculated from the training sample (dots for dwarf stars and squares for giant stars). Different symbol colors indicate the metallicity determined from different stellar colors.



**Figure 5.** Metallicity difference (photometric minus spectroscopic), as a function of SFD98 E(B-V), for over 600,000 and 200,000 LAMOST dwarf (top) and giant (bottom) stars, respectively. The blue squares and error bars in each panel represent the median and dispersion of the metallicity differences in the individual E(B-V) bins. The red dashed lines in each panel represent the best-fit fifth-order polynomials to the trends of metallicity differences with E(B-V).

Collaboration et al. 2021). The Gaia EDR3 broadband photometry is essentially complete between G=12 and G=17. The completeness is quite complicated for sources fainter than G=17, which is strongly dependent on celestial position (Riello et al. 2021; Cantat-Gaudin et al. 2023; Castro-Ginard et al. 2023). In total, nearly 33 million stars are selected by the following cuts:

- 1. flag\_u/v = 0 in SAGES DR1;
- 2. Uncertainties of G,  $G_{\rm BP}$ , and  $G_{\rm RP}$  smaller than 0.05 mag;
- 3. Galactic latitude  $|b| \ge 10^{\circ}$ .

SAGES was initially designed to avoid the high-reddening regions with  $|b| \le 10^\circ$ , although a few disk areas are observed for specific reasons. The former two cuts are required for precise metallicity estimates, but they do affect the completeness in the faint range (G > 18.5). The last cut is to exclude those disk regions in our analysis, given their high values of extinction. This sample is referred to as the main sample for our following analysis.

In this study, the colors  $u - G_{\rm BP}$ ,  $v - G_{\rm RP}$ , and  $G_{\rm BP} - G_{\rm RP}$  are used. We note that the mean  $G_{\rm BP}$  flux in Gaia EDR3 is overestimated for faint red sources with  $G \geqslant 20.0$  (e.g., Riello et al. 2021; Onken et al. 2022). However, only 650,000 stars (no more than 3% of the full sample) in our final catalog are fainter than the 20th magnitude in the G band. Therefore, the systematic issue for  $G_{\rm BP}$  is minor for the current study. Unless indicated otherwise, these colors are corrected for reddening using the extinction map of Schlegel et al. (1998, hereafter SFD98). The reddening coefficients for those colors, as well as for the G band, are calculated using the same way as in H22.

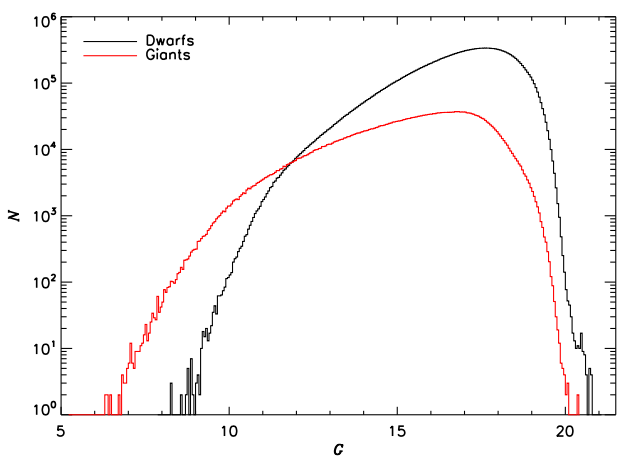
# 3. Metallicity Determination

#### 3.1. Training Set

The key to determinations of metallicity using stellar colors is the training set. The training set adopted here is similar to that used in H22, which consists of (1) LAMOST DR9,  $^{12}$  (2) the revised parameters of metal-poor ([Fe/H]  $\leq$  -1.8) stars of SEGUE (Yanny et al. 2009; Rockosi et al. 2022), along with other data sets from SDSS (we refer to the total data set below

Here the SFD98 E(B-V) is corrected for a 14% systematic overestimate (e.g., Schlafly & Finkbeiner 2011; Yuan et al. 2013).

<sup>&</sup>lt;sup>2</sup> http://www.lamost.org/dr9/v1.0/



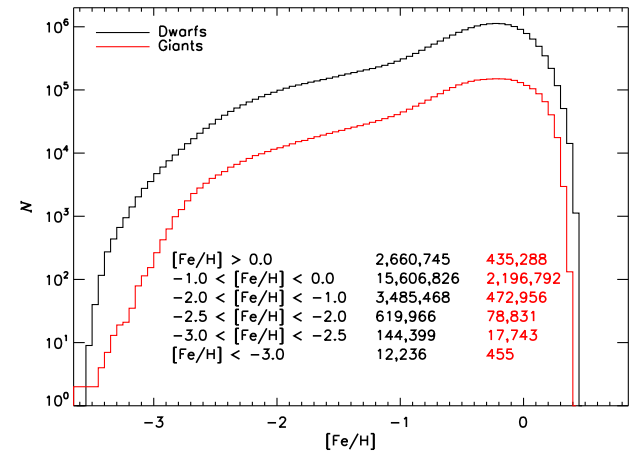


**Figure 6.** Left panel: magnitude distributions of dwarf (black line) and giant (red line) stars with photometric metallicity estimated from the colors provided by SAGES DR1 and Gaia EDR3. Right panel: distributions of photometric metallicity for dwarf (black line) and giant (red line) stars. The number of dwarf (black) and giant (red) stars included in individual metallicity bins are marked.

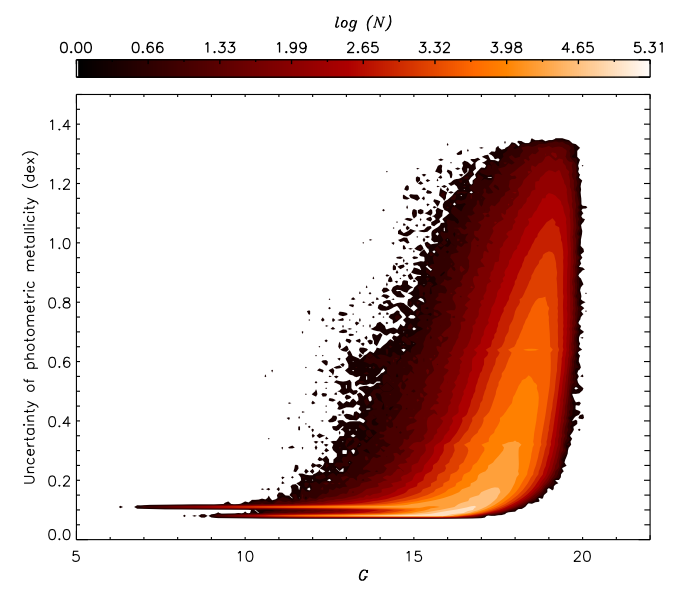


**Figure 7.** Density map (on a logarithmic scale) of the uncertainties of photometric-metallicity estimates vs. *G*-band magnitude.

as SEGUE), and LAMOST (Deng et al. 2012; Liu et al. 2014) by a custom version of the SSPP (LSSPP; Lee et al. 2015), along with careful visual inspection (by Beers), and (3) the bibliographical compilation of measurements of stellar atmospheric parameters from high-resolution spectroscopy (HRS) by PASTEL (Soubiran et al. 2016) and SAGA (Suda et al. 2008). The metallicity scale of the former two sets is calibrated to the one obtained from the HRS data set. More details of our efforts to construct a training set with a homogenous scale of metallicity, as well as other elemental-abundance ratios, will be described in Y. Huang et al. (2023, in preparation).

We then crossmatch the above training set to the main sample, together with the following cuts:

- 1. The stars must have small values of extinction (to minimize uncertainties due to reddening corrections): Galactic latitude  $|b| \ge 20^{\circ}$  and  $E(B-V) \le 0.08$ ;
- 2. The stars must have reliable metallicity estimates: LAMOST/SEGUE spectral signal-to-noise ratio (S/N) greater than 20, effective temperatures in the range 3800  $\leq T_{\rm eff}$  (K)  $\leq$  7500 (i.e., typical FGK-type stars);

- 3. The photometric uncertainties in the SAGES uv and Gaia  $G_{\rm BP}G_{\rm RP}G$  bands must be smaller than 0.035 mag;
- 4. The stars must have Gaia relative parallax measurement uncertainties smaller than 50%.

In addition to the above cuts, only about half of the metal-rich ([Fe/H] > -1.0) stars are selected to avoid large differences in the number of metal-rich ([Fe/H] > -1.0) and metal-poor ([Fe/H] < -1.0) stars (see the right panel of Figure 1). Given the number of stars in common between SAGES and those with spectroscopy, the cut on Galactic latitude would not introduce bias in the training sets, e.g., a lack of metal-rich disk populations (see the right panel of Figure 1). A total of 223,537 stars (182,035 dwarfs and 41,502 giants) are selected to construct the final training set. The absolute G-band magnitudes of these stars are derived by adopting the distances from Bailer-Jones et al. (2021), based on the parallax measurements from Gaia EDR3. The Hertzsprung-Russell (H-R) diagram of the training set is then shown in the left panel of Figure 1. By using empirical cuts defined in H22, the training stars are further divided into dwarf and giant stars. The right panel of Figure 1 shows the metallicity distributions of the dwarf and giant stars in the training set.

# 3.2. Metallicity Estimation

To estimate photometric metallicity, we first define the metallicity-dependent stellar loci of  $(u/v-G_{\rm BP})_0$  versus  $(G_{\rm BP}-G_{\rm RP})_0$  in Figure 2 for both dwarf stars (top panel) and giant stars (bottom panel). Similar to our results with SMSS DR2 in H22, both  $(u-G_{\rm BP})_0$  and  $(v-G_{\rm BP})_0$  colors exhibit significant sensitivities to stellar metallicity for different types of stars characterized by  $(G_{\rm BP}-G_{\rm RP})_0$ . Third-order 2D polynomials with 10 free parameters are then applied to describe the stellar loci of dwarf and giant stars:

$$(u/v - G_{BP})_0 = a_{0,0} + a_{0,1}y + a_{0,2}y^2 + a_{0,3}y^3 + a_{1,0}x + a_{1,1}xy + a_{1,2}xy^2 + a_{2,0}x^2 + a_{2,1}x^2y + a_{3,0}x^3,$$
(1)

where x and y represent  $(G_{\rm BP}-G_{\rm RP})_0$  and [Fe/H], respectively.  $2\sigma$ -3 $\sigma$  clipping is applied in the fitting process. The resultant fit coefficients are listed in Table 1.

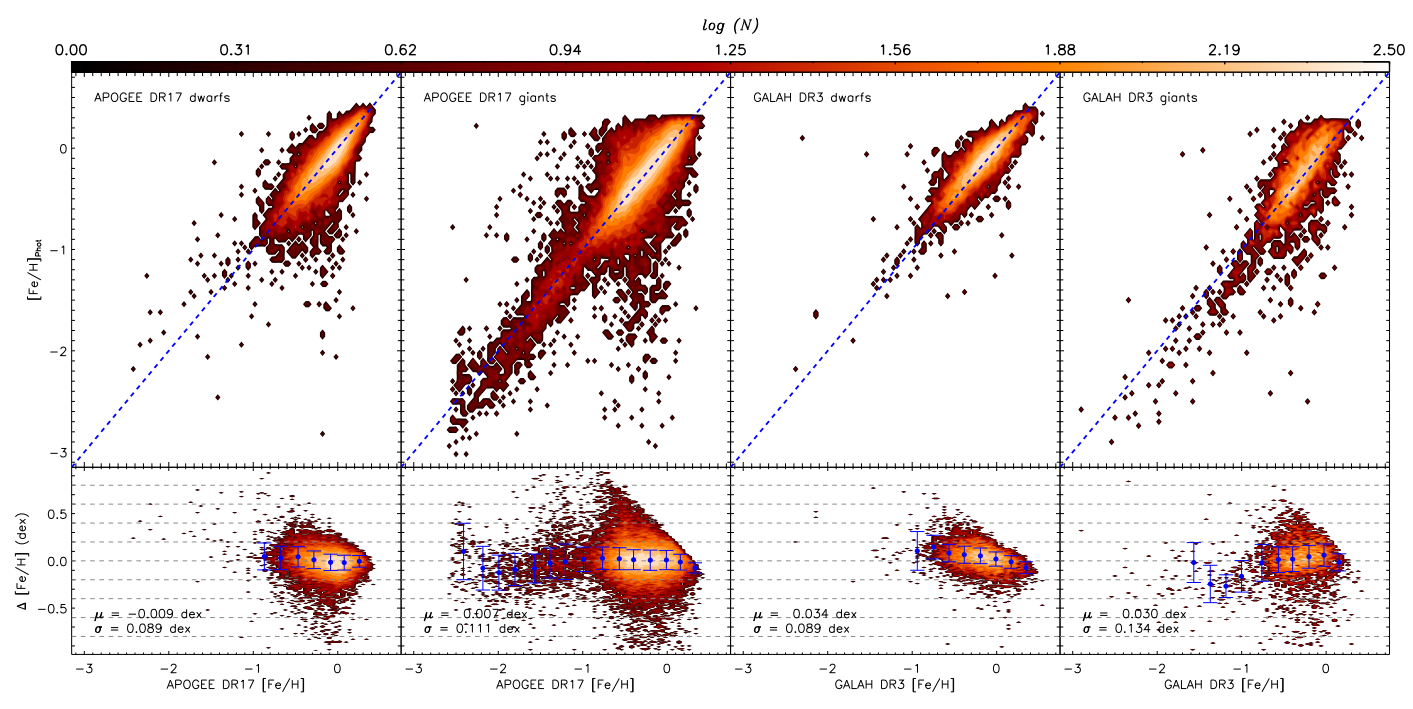
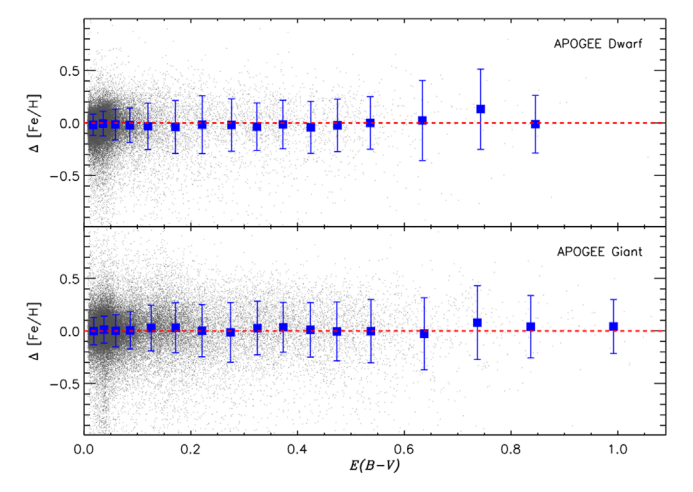


Figure 8. Comparisons of photometric-metallicity estimates with high-resolution spectroscopic metallicities from APOGEE DR17 (left two panels) and GALAH DR3 + (right two panels). The metallicity differences (photometric minus spectroscopic) are shown in the lower panels, with the overall median and standard deviation marked in the bottom-left corners. In each panel, a color-coded contour of the stellar number density on a logarithmic scale is shown. The blue dots and error bars in each panel indicate the medians and dispersions of the metallicity differences in the individual metallicity bins.



**Figure 9.** Similar to Figure 5, but for APOGEE stars. Here, the E(B-V) dependent offsets, as found in Figure 5, have been corrected to obtain the photometric-metallicity estimates.

Using the stellar loci, one can determine the photometric metallicity using the maximum-likelihood approach developed in H22. For a given star, the metallicity is obtained from the probability distribution function (pdf) of [Fe/H] estimated from the likelihood function:

$$L_c = \frac{1}{\sqrt{2\pi}\sigma_{\text{cobs}}} \exp \frac{-(c_{\text{obs}} - c_{\text{pred}})^2}{2\sigma_{\text{cobs}}^2},$$
 (2)

where  $c_{\rm obs}$  are the observed colors, i.e.,  $(u/v-G_{\rm BP})_0$ , with assumed Gaussian errors  $\sigma_{c_{\rm obs}}$ . The  $c_{\rm pred}$  represents the same colors predicted by the metallicity-dependent stellar loci (defined by Equation (1)) with  $(G_{\rm BP}-G_{\rm RP})_0$  from observations and [Fe/H] ranging from -3.5 to +0.8 in steps of 0.01 dex. The uncertainty in the photometric metallicity

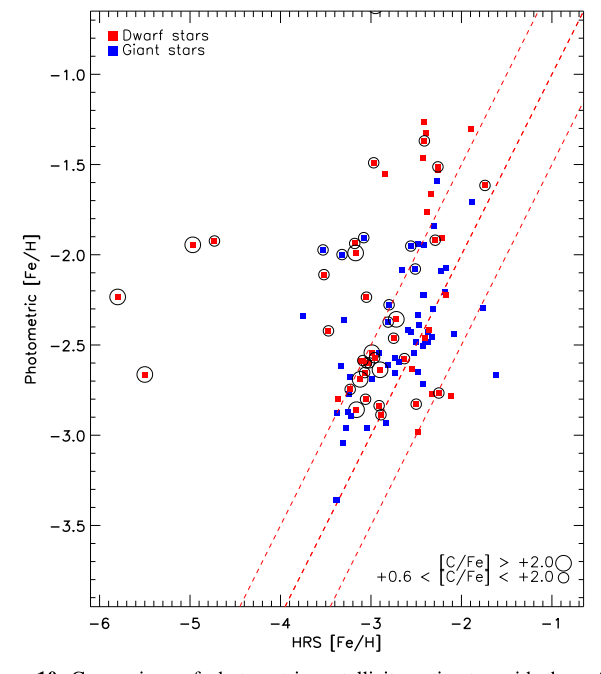
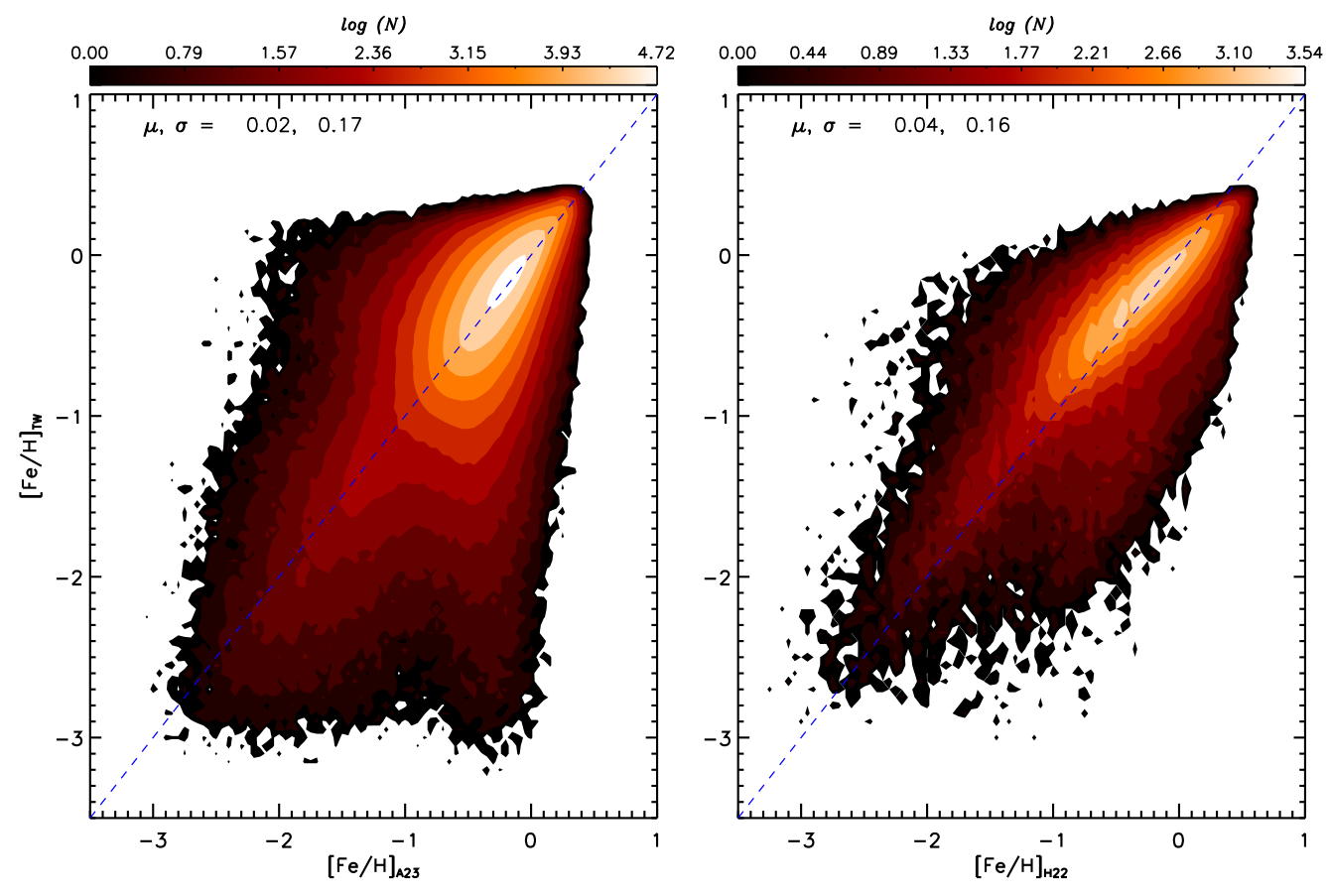


Figure 10. Comparison of photometric-metallicity estimates with those from the high-resolution spectroscopic metallicities for dwarf (red squares) and giant (blue squares) stars. The HRS samples we compare with include a sample of the most metal-poor stars (Norris & Yong 2019), the *R*-Process Alliance sample (Hansen et al. 2018; Sakari et al. 2018; Ezzeddine et al. 2020; Holmbeck et al. 2020) for over 600 VMP stars, the CFHT ESPaDONS follow-up observations of 132 metal-poor candidates selected from the Pristine survey (Lucchesi et al. 2022), the Subaru follow-up observations of 400 VMP candidates selected from the LAMOST (Aoki et al. 2022; Li et al. 2022), and the GTC follow-up observations of extremely metal-poor candidates identified from the Pristine and LAMOST surveys (Arentsen et al. 2023). The small and large circles mark stars with carbon enhancements (+0.6 < +0.6 < +0.6 < +0.6 < +0.6 < +0.6 < +0.6 < +0.6 < +0.6 < +0.6 < +0.6 < +0.6 < +0.6 < +0.6 < +0.6 < +0.6 < +0.6 < +0.6 < +0.6 < +0.6 < +0.6 < +0.6 < +0.6 < +0.6 < +0.6 < +0.6 < +0.6 < +0.6 < +0.6 < +0.6 < +0.6 < +0.6 < +0.6 < +0.6 < +0.6 < +0.6 < +0.6 < +0.6 < +0.6 < +0.6 < +0.6 < +0.6 < +0.6 < +0.6 < +0.6 < +0.6 < +0.6 < +0.6 < +0.6 < +0.6 < +0.6 < +0.6 < +0.6 < +0.6 < +0.6 < +0.6 < +0.6 < +0.6 < +0.6 < +0.6 < +0.6 < +0.6 < +0.6 < +0.6 < +0.6 < +0.6 < +0.6 < +0.6 < +0.6 < +0.6 < +0.6 < +0.6 < +0.6 < +0.6 < +0.6 < +0.6 < +0.6 < +0.6 < +0.6 < +0.6 < +0.6 < +0.6 < +0.6 < +0.6 < +0.6 < +0.6 < +0.6 < +0.6 < +0.6 < +0.6 < +0.6 < +0.6 < +0.6 < +0.6 < +0.6 < +0.6 < +0.6 < +0.6 < +0.6 < +0.6 < +0.6 < +0.6 < +0.6 < +0.6 < +0.6 < +0.6 < +0.6 < +0.6 < +0.6 < +0.6 < +0.6 < +0.6 < +0.6 < +0.6 < +0.6 < +0.6 < +0.6 < +0.6 < +0.6 < +0.6 < +0.6 < +0.8 <+0.8 <+0.8 <+0.8 <+0.8 <+0.8 <+0.8 <+0.8 <+0.8 <+0.8 <+0.8 <+0.8 <+0.8 <+0.8 <+0.8 <+0.8 <+0.8 <+0.8 <+0.8 <+0.8 <+0.8 <+0.8 <+0.8 <+0.8 <+0.8 <+0.8 <+0.8 <+0.8 <+0.8 <+0.8 <+0.8 <+0.8 <+0.8 <+0.8 <+0.8 <+0.8 <+0.8 <+0.8 <+0.8 <+0.8 <+0.8 <+0.8 <+0.8 <+0.8 <+0.8 <+0.8 <+0.8 <+0.8 <+0.8 <+0.8 <+0.8 <+0.8 <+0.8 <+0.8 <



**Figure 11.** Comparison of estimated photometric metallicity, [Fe/H], from this work with that derived by (Andrae et al. 2023, A23) for over five million stars in common (left panel), and that derived by H22 for about 390,000 stars in common (right panel). The color-coded contours of the stellar number density are shown with color bars on the top of each panel. The values of median and standard deviation of the metallicity differences (this work minus A23/H22) are marked in the top-left corners.

estimated is taken to be half of the 68% interval of the resultant pdf.

From the above approach, we estimate the photometric metallicities of training-set stars to be compared to the spectroscopic measurements as an internal test. These comparisons are shown in Figure 3 for both dwarf stars (top panel) and giant stars (bottom panel). Generally, the estimated photometric metallicities agree with the spectroscopic metallicities very well for both dwarf and giant stars, either from  $(u - G_{BP})_0$  or  $(v - G_{\rm BP})_0$ ; the overall scatter is only 0.09 and 0.13 dex for dwarf stars achieved by  $(u - G_{BP})_0$  and  $(v - G_{BP})_0$ , respectively. The scatter of the combined estimates using an errorweighted mean is further reduced to 0.08 dex, even better than the precision of low/medium-resolution spectroscopy. As shown in the top-right panel of Figure 4, no significant systematic offset is found for dwarf stars with photometric [Fe/H] > -1.0, and a mild offset of -0.20 to -0.4 dex (photometric minus spectroscopic) is found for metal-poor dwarf stars with photometric  $[Fe/H] \le -1.0$ . The metallicity precision for dwarf stars as revealed by the internal comparisons is a function of [Fe/H], with scatter smaller than 0.1 dex for [Fe/H] > -0.5, increasing to 0.3–0.4 dex at the extremely metal-poor end ([Fe/H]  $\sim$ -3.0). For giant stars, the overall scatter is around 0.11 dex. The comparisons show that photometric metallicity derived from  $(v - G_{\rm BP})_0$  is in excellent agreement with that of spectroscopy, with negligible offsets for [Fe/H] > -2.0 and a small offset of  $-0.2 \,\mathrm{dex}$  (photometric minus spectroscopic) at the extremely metal-poor end ([Fe/H]  $\sim -3.0$ ). The metallicity precision from

 $(v-G_{\rm BP})_0$  is around 0.1 dex for [Fe/H] >-1.0, and 0.2-0.3 dex for [Fe/H]  $\le-1.0$ . The performance of photometric metallicity derived from  $(u-G_{\rm BP})_0$  is moderately worse, especially for warmer giant stars, which are mostly blue horizontal-branch stars (see the blue box in the bottom-left panel of Figure 3). Finally, the internal checks indicate that there are no systematic trends with effective temperature for the photometric-metallicity estimates of both dwarf and giant stars (see the top-left panel of Figure 4).

In addition to the internal test, we derive photometric metallicities for LAMOST targets with larger values of E(B-V) that are not included in the training set. Using the LAMOST targets (including these stars with low values of extinction in the training set), we show the metallicity differences between the photometric and spectroscopic values as a function of E(B-V) in Figure 5. The metallicity differences (photometric minus spectroscopic) steadily decrease with E(B-V), and reach  $\sim +0.2$  dex at  $E(B-V) \sim 0.5$  for both dwarf and giant stars. This trend is possibly due to the spatial systematic uncertainties of the SFD98 extinction map, as found most recently by Sun et al. (2022). Moreover, Zhang & Yuan (2023) have shown that the reddening coefficients depend not only on effective temperature/intrinsic colors, but also extinction itself (ignored in this work). The neglect of the extinction term may also partly contribute to this E(B-V) dependent trend. To correct for this systematic trend, a fifth-order polynomial is applied to describe

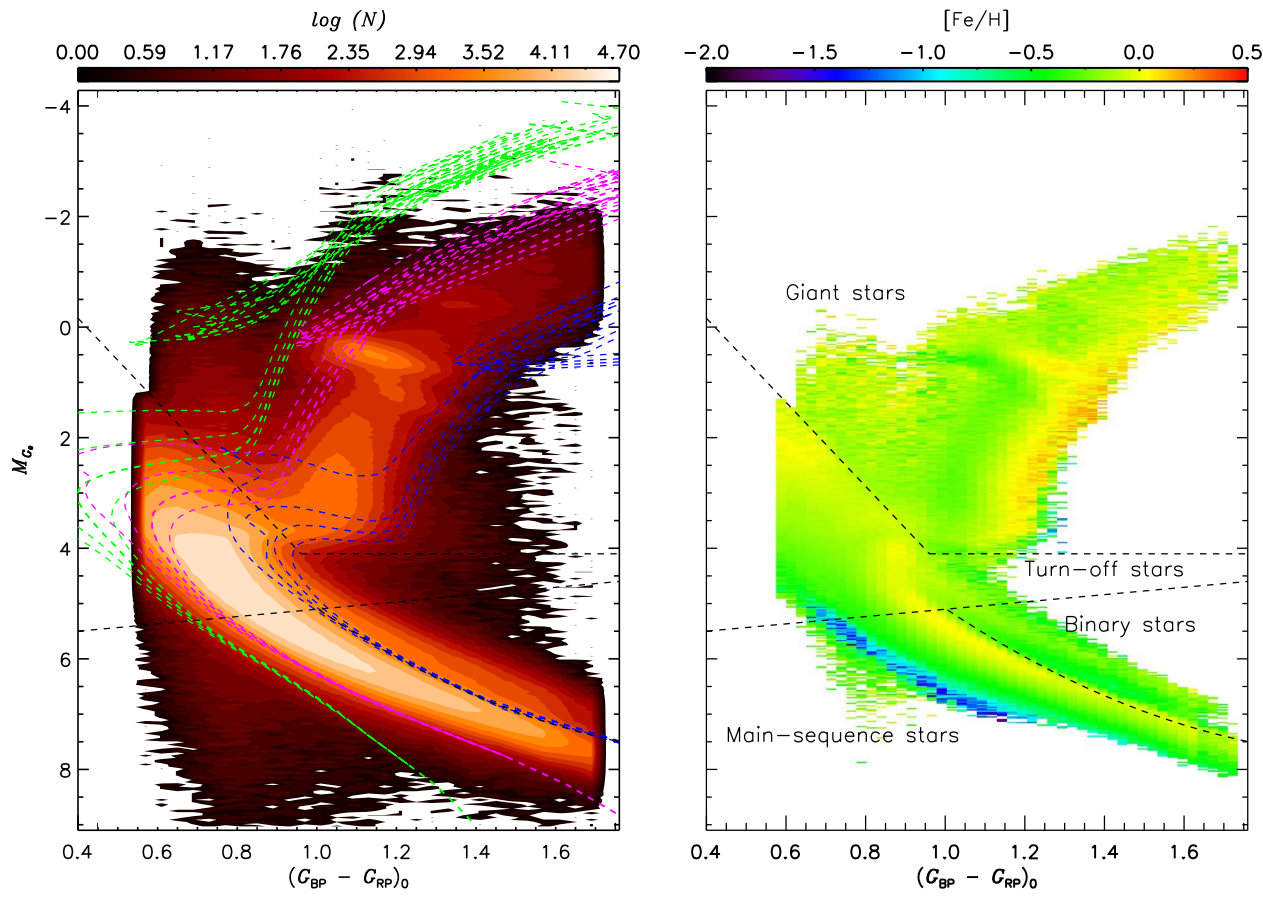


**Figure 12.** Left panel: number-density distribution (on a logarithmic scale) in the H-R diagram:  $M_{G_0}$  vs.  $(G_{BP} - G_{RP})_0$ . The blue, magenta, and green dashed lines represent stellar isochrones from PARSEC (Bressan et al. 2012; Marigo et al. 2017) with total metallicity [M/H] = +0.50, -0.75, and -2.00. Isochrones of the same colors have different ages, from 3 to 9 Gyr, in steps of 2 Gyr (from left to right). The upper black dashed lines (defined in Figure 1) are used to classify dwarf and giant stars. The middle dashed line marks the main-sequence turn-off stars (above this line). The lower dashed line separates main-sequence (left part) and likely binary stars (right part). Right panel: similar to the left panel, but color coded with the median photometric [Fe/H], as indicated by the top color bar.

the differences as a function of E(B-V) for dwarf and giant stars, respectively.

According to the above tests, the final metallicity of a dwarf star is given by the combined estimate if both  $(u-G_{\rm BP})_0$  and  $(v-G_{\rm BP})_0$  colors are available, or given by the single measurement from either  $(u-G_{\rm BP})_0$  or  $(v-G_{\rm BP})_0$ , depending on which color is available. The final metallicity of a giant star is given by the measurement of color  $(v-G_{\rm BP})_0$ , or the color  $(u-G_{\rm BP})_0$  if the former is not available. In this manner, photometric-metallicity estimates are derived for over 26 million stars (23 million dwarf stars and 3 million giant stars) in SAGES. Note that the extinction dependent zero-point offsets are corrected using the fifth-order polynomial constructed above. The G-band magnitude distributions of stars with metallicity estimates are shown in the left panel of Figure 6.

The overall completeness limit is around magnitudes G = 17.5 and 18.5, for dwarf and giant stars, respectively. As mentioned earlier, we caution that the completeness of Gaia broadband photometry is quite complicated, especially in crowded regions, for stars with G > 17 (Riello et al. 2021; Cantat-Gaudin et al. 2023; Castro-Ginard et al. 2023). The photometric-metallicity distributions of dwarf and giant stars are shown in the right panel of Figure 6. The total number of very metal-poor (VMP; [Fe/H] < -2.0) stars is about one million, which is the largest database of VMP candidates yet

assembled from photometric techniques. The metallicity uncertainty of a star is contributed by two sources: the method error deduced from the internal checks and the random errors derived from the likelihood function. The metallicity uncertainty as a function of *G*-band magnitude is shown in Figure 7, which is dominated by the method error and random errors in the bright and faint end, respectively.

## 3.3. Comparison with APOGEE DR17 and GALAH DR3+

The accuracy of our photometric estimates of metallicity is examined by comparisons with the independent spectroscopic measurements from the APOGEE DR17 (Abdurro'uf et al. 2022) and GALAH DR3+ (Buder et al. 2021). The comparisons are shown in Figure 8 for 72,995 high-quality  $(S/N \ge 30)$  stars in common with APOGEE and 13,038 highquality  $(S/N \ge 30)$  stars in common with GALAH DR3+. Generally, the photometric-metallicity estimates agree very well with the spectroscopic values, without significant offsets. The overall scatter is only 0.09 dex for dwarf stars and 0.10-0.15 dex for giant stars. The zero-point and precision of individual metallicity bins are also examined in the lower panels of Figure 8; the results are consistent with our internal tests (see Figure 4). We also present the metallicity differences between the photometric estimates and spectroscopic values from APOGEE DR17 as a function of E(B-V) in Figure 9. The plot clearly shows that the offsets are all around zero for

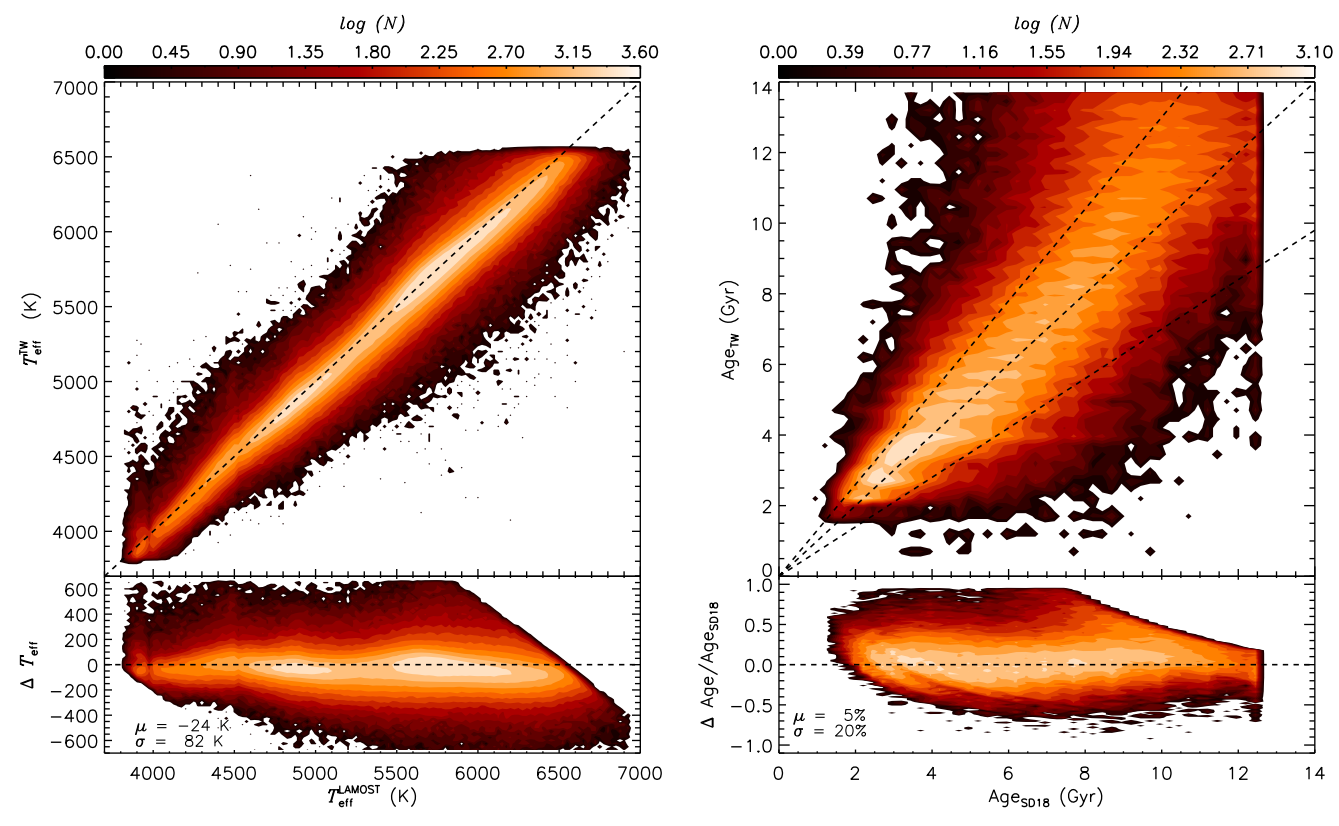


Figure 13. Left panel: comparisons of effective temperature measurements between this work and LAMOST for over 159,000 stars in common. The lower panel shows the effective temperature difference (this work minus LAMOST), as a function of LAMOST effective temperature, with the values of the median and standard deviation of the effective temperature difference marked in the bottom-left corner. Right panel: comparisons of stellar-age estimates between this work and Sanders & Das (2018; SD18) for over 160,000 main-sequence turn-off stars in common. The dashed lines indicate  $Age_{TW} = 0.7$ , 1.0, and 1.3 times of  $Age_{SD18}$ . The lower panel shows the relative age difference (this work minus SD18), as a function of SD18 age, with the values of the median and standard deviation of the relative age difference marked in the bottom-left corner. In each panel, a color-coded contour of the stellar number density on a logarithmic scale is shown.

different bins of E(B-V), a validation of our polynomial corrections described in Section 3.2 (see Figure 5).

# 3.4. Comparison with Metal-poor Samples from Highresolution Spectroscopy

To explore the capabilities of the SAGES filters for determinations of metallicity for metal-poor stars, we collect samples of independent metallicity estimates from HRS, especially for metal-poor stars. The HRS samples we compare with include a sample of the most metal-poor stars (Norris & Yong 2019), the *R*-Process Alliance sample (Hansen et al. 2018; Sakari et al. 2018; Ezzeddine et al. 2020; Holmbeck et al. 2020) for over 600 VMP stars, the CFHT ESPaDOnS follow-up observations of 132 metal-poor candidates selected from the Pristine survey (Lucchesi et al. 2022), the Subaru follow-up observations of 400 VMP candidates selected from the LAMOST (Aoki et al. 2022; Li et al. 2022), and the Gran Telescopio Canarias (GTC) follow-up observations of extremely metal-poor candidates identified from the Pristine and LAMOST surveys (Arentsen et al. 2023).

We crossmatch the SAGES sample to the collected HRS samples and find 112 stars in common (54 dwarfs and 58 giant stars). The comparison result is shown in Figure 10. Generally, our photometric-metallicity estimates are consistent with the HRS values for metal-poor stars without significant carbon enhancements ([C/Fe] < +0.6). The overall scatter of the differences (photometric minus spectroscopic) is 0.57 and 0.30 dex, respectively, for dwarf and giant stars, with mild

offsets of +0.38 and +0.18 dex, respectively. The result is in line with our internal checks (see Figure 4). We note the photometric-metallicity estimates of ultra-metal-poor ([Fe/H] <-4.0) stars can be overestimated by up to 2 dex for stars with very high carbon enhancements ([C/Fe]  $\geqslant +2.0$ ).

# 3.5. Comparison with SMSS and Gaia XP Spectra

We compare our results to those of H22 from SMSS and those of Andrae et al. (2023) from Gaia XP<sup>13</sup> low-resolution spectra. The latter has recently delivered estimates of metallicity using a data-driven technique for over 120 million stars from Gaia XP low-resolution spectra. As shown in Figure 11, our estimates are consistent with those of Andrae et al. (2023) and H22, with tiny offsets and a scatter smaller than 0.20 dex. Finally, although the total number of our metallicity estimates (SAGES + SMSS) does not exceed 50 million stars, we emphasize that the volume of our sample is much larger than that of sample constructed from Gaia XP spectra, given that the limiting magnitude of SAGES and SMSS is nearly 3 mag deeper than that of the Gaia XP spectra. This larger volume will enable numerous interesting studies of the Milky Way, e.g., searching for substructures in the stellar halo.

## 4. Effective Temperature, Distance, and Age Estimates

The effective temperatures of dwarf and giant stars are derived from the metallicity-dependent  $T_{\rm eff}$ -color relations

 $<sup>\</sup>overline{^{13}}$  Here XP spectra represents the Gaia BP and RP spectra.

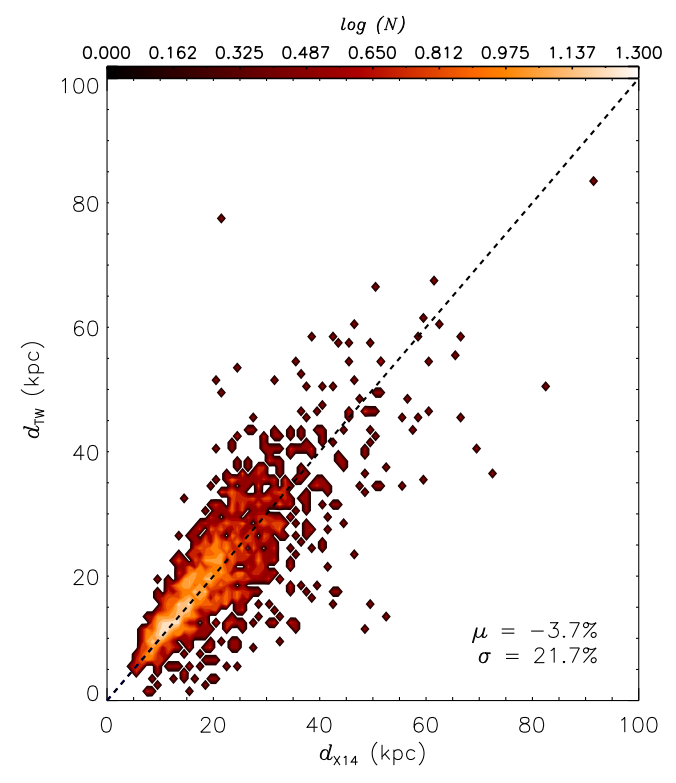


**Figure 14.** Comparison of photometric distances estimated using the likelihood method in this work to those from Xue et al. (2014). The color-coded contour of the stellar number density is shown with color bars on the top of each panel. The overall relative median offset and standard deviation of the distance difference are marked in the bottom-right corner.

constructed in H22. Here the color is the dereddened  $(G_{\rm BP}-G_{\rm RP})_0$ , and metallicity is given by photometric [Fe/H]. In this way, effective temperatures are obtained for all of our program stars. As examined with over 159,000 stars in common, the effective temperature estimated in this work is quite consistent with that from LAMOST, with a small offset around  $-24~\rm K$  (this work minus LAMOST) and a scatter of only 84 K (see Figure 13).

Distances estimated by Bailer-Jones et al. (2021) are adopted for stars with reliable parallax measurements with precision better than 30%, parallax greater than 0.15 mas, and renormalized unit weight error (RUWE) smaller than 1.4. A total of 15,974,812 stars have distances estimated in this way. Using the apparent G-band magnitudes and SFD98 E(B-V), the G-band absolute magnitudes have been derived for the nearly 16 million stars with reliable geometric distances. Figure 12 is the H-R diagram for about eight million stars with relative parallax error better than 10%, parallax greater than 0.4 mas, and RUWE  $\leq$ 1.4. Guided by the isochrones of PARSEC (Bressan et al. 2012; Marigo et al. 2017), empirical cuts are defined to further classify dwarf stars into main-sequence turnoff, main-sequence, and binary stars.

For the stars without geometric distance estimates, the distances are obtained by inferring their absolute magnitudes from the constraints of stellar colors and photometric metallicity. For main-sequence dwarf stars, the *G*-band absolute magnitudes are derived from the third-order 2D polynomial relation constructed in H22. Combining with the *G*-band magnitude and the SFD E(B-V), the distances are found for over one million main-sequence dwarf stars with  $(G_{BP}-G_{RP})_0 \ge 1.0$ .

Table 2
Sample Content

	Dwarf	Giant	All
Total	22,529,640	3,202,065	25,731,705
Stars with [Fe/H] measurements	22,529,640	3,202,065	25,731,705
[Fe/H] measured by $u - G_{BP}$	5,955,809	814,066	6,769,875
[Fe/H] measured by $v - G_{\rm BP}$	2,611,929	2,387,999	4,999,928
[Fe/H] measured by two colors	13,961,902	•••	13,961,902
Stars with $T_{\rm eff}$ measurements	22,529,640	3,202,065	25,731,705
Stars with distance measurements	14,690,031	2,951,337	17,641,368
Distance estimated by Gaia EDR3 parallax	13,595,147	1,409,144	15,004,291
Distance estimated by color-absolute magnitude fiducials	1,094,884	1,542,193	2,637,077
Stars with age measurements	13,428,487	1,365,693	14,794,180
Stars with RV measurements	3,045,883	1,168,081	4,213,964
RV measured from GALAH DR3+	24,261	11,918	36,179
RV measured from APO- GEE DR17	43,983	56,927	1,100,910
RV measured from Gaia DR3	2,038,911	1,001,874	3,040,785
RV measured from RAVE DR5	25	11	36
RV measured from LAMOST DR9	836,516	87,902	924,418
RV measured from SDSS/ SEGUE DR16	102,187	9449	111,636

Notes. The bold value is intended to highlight the total number of parameters.

For giant stars, a likelihood method developed in (Xue et al. 2014, hereafter X14) and Huang et al. (2019) is adopted to infer the i-band absolute magnitude using the  $(g-i)_0$  color, photometric [Fe/H], and empirical color–magnitude fiducials interpolated from six globular clusters. Here, the g- and i-band magnitudes are from the Pan-STARRS1 surveys (Chambers et al. 2016); the reddening-correction coefficients are from Green et al. (2019). The interested reader is referred to X14 or Huang et al. (2019) for more details.

In the above manner, a total of over 1.6 million giant stars have their distances estimated. To test the accuracies of our distance estimates for giant stars, Figure 14 compares these with those of X14 for over 1600 stars in common. The results are consistent with each other, with a tiny relative offset of -3.7% (this work minus X14) and a scatter of 21.7%. This scatter implies that both estimates have a typical precision of about 16%, which is expected by X14.

Finally, we derive stellar ages for stars with good parallax measurements, i.e., parallax measurements with precision better than 30%, parallax greater than 0.15 mas, and RUWE ≤1.4, using the technique developed in H22. Nearly 15 million stars have their ages estimated in this way. We note that the RUWE cut cannot exclude all of the binary stars, whose ages may be overestimated. As noted by H22, this technique is mostly valid for main-sequence turn-off and subgiant stars; uncertainties are larger for other types of stars in the H-R diagram. We perform a similar check as done in H22 with over 160,000 stars in common between this work and (Sanders & Das 2018, SD18), who derived isochrone ages for over three million stars with both spectroscopic and astrometric information. The check shows that the age estimates in this work agree with with those from SD18, with an offset of 5% in relative age

**Table 3**Description of the Final Sample

Field	Description	Unit
Sourceid	Gaia EDR3 source ID	
ra	R.A. from SAGES DR1 (J2000)	deg
dec	decl. from SAGES DR1 (J2000)	deg
gl	Galactic longitude derived from ICRS coordinates	deg
gb	Galactic latitude derived from ICRS coordinates	deg
u/v	Magnitudes for the SAGES two bands from SAGES DR1	
err_u/v	Uncertainties magnitudes for the SAGES two bands from SAGES DR1	mag
g/r/i	Magnitudes from Pan-STARRS1	
err_g/r/i	Uncertainties of magnitudes from Pan-STARRS1	mag
G/BP/RP	Magnitudes for the Gaia three bands from EDR3; note G represents a calibration-corrected G magnitude	
err_G/BP/RP	Uncertainties of magnitudes for the three Gaia bands from EDR3	mag
ebv_sfd	Value of $E(B-V)$ from the extinction map of SFD98, corrected for a 14% systematic	
$BR_0/uB_0/vB_0$	Intrinsic colors of $(G_{BP} - G_{RP})_0$ , $(u - G_{BP})_0$ , and $(v - G_{BP})_0$	_
$err_BR_0/uB_0/vB_0$	Uncertainties of intrinsic colors of $(G_{BP} - G_{PP})_0$ , $(u - G_{BP})_0$ , and $(v - G_{BP})_0$	mag
[Fe/H]	Photometric metallicity	
err_[Fe/H]	Uncertainty of photometric metallicity	dex
flg_[Fe/H]	Flag to indicate the stellar color(s) used in estimating [Fe/H], which takes the values "ub," "vb," and "ub+vb"	
$T_{\rm eff}$	Effective temperature	K
$err_T_{eff}$	Uncertainty of effective temperature	K
dist_adop	Distance	kpc
err dist adop	Uncertainty of distance	kpc
dist_adop_flg	Flag to indicate the method used to derive distance, which takes the values "parallax," "CMF," and "NO"	
X/Y/Z	3D positions in the right-hand Cartesian system	kpc
err_X/Y/Z	Uncertainties of 3D positions in the right-hand Cartesian system	kpc
$R_{\rm GC}$	Galactocentric distance	kpc
err_R <sub>GC</sub>	Uncertainty of Galactocentric distance	kpc
R	Projected Galactocentric distance onto the Galactic plane	kpc
err R	Uncertainty of projected Galactocentric distance	kpc
age	Stellar age	Gyr
err_age	Uncertainty of stellar age	Gyr
rv_adop	Radial velocity	$km s^{-1}$
err rv adop	Uncertainty of radial velocity	$km s^{-1}$
rv_adop_flg	Flag to indicate the source of radial velocity, which takes the values "GALAH," "APOGEE," "Gaia,"	
r,_udop_ng	"RAVE," "LAMOST," "SEGUE"	
parallax	Parallax from Gaia EDR3	mas
err_parallax	Uncertainty of parallax from Gaia EDR3	mas
pmra	Proper motion in R.A. direction from Gaia EDR3	mas yr <sup>-1</sup>
err_pmra	Uncertainty of proper motion in R.A. direction from Gaia EDR3	mas yr <sup>-1</sup>
pmdec	Proper motion in decl. direction from Gaia EDR3	mas yr <sup>-1</sup>
err_pmdec	Uncertainty of proper motion in decl. direction from Gaia EDR3	mas yr <sup>-1</sup>
ruwe	Renormalized unit weight error from Gaia EDR3	
type	Flag to indicate classifications of stars, which takes the values "dwarf" and "giant"	
subtype	Flag to indicate further subclassifications of dwarf stars, which takes the values "TO," "MS," and "Binary"	•••

difference (age $_{\rm TW}-$  age  $_{\rm SD18})/{\rm age}_{\rm SD18}$  and a scatter in the relative age difference of around 20%.

## 5. Radial Velocities and the Final Sample

We collect measurements of radial velocities for our sample stars available from from completed and ongoing spectroscopic surveys, including GALAH DR3+ (Buder et al. 2021), SDSS/APOGEE DR17 (Abdurro'uf et al. 2022), Gaia DR3 (Katz et al. 2023), RAVE DR5 (Kunder et al. 2017), LAMOST DR9, <sup>14</sup> and SDSS/SEGUE DR16 (Ahumada et al. 2020), with typical measurement errors of 1.1, 0.5, 1.0–6.0, 2.0, 5.0, and 5.0 km s<sup>-1</sup>, respectively. In total, over 4.2 million stars in our final sample have radial-velocity measurements. The detailed contributions of radial velocities from each survey are given in

Table 2. If a star has radial-velocity measurements from two more surveys, the result from the survey with the highest spectral resolution is adopted. We note that all of the radial-velocity zero-points are calibrated to the updated APOGEE radial-velocity standard stars based on the SDSS/APOGEE DR17 constructed using the same technique proposed in Huang et al. (2018).

In the final sample, over 22 million dwarf and 3 million giant stars have photometric-metallicity estimates (see Section 3) from the stellar colors provided by SAGES DR1 (Fan et al. 2023) and Gaia EDR3 (Gaia Collaboration et al. 2021), and effective temperature estimates from the intrinsic  $(G_{\rm BP}-G_{\rm RP})_0$  colors and photometric [Fe/H] (see Section 4). From the well-developed techniques described in H22, distances and ages are further derived for 18 and 15 million stars in the final sample, respectively (see Section 4). The radial-velocity measurements, if available from the spectroscopic

<sup>14</sup> http://www.lamost.org/dr9/v1.0/

surveys, and the astrometric parameters in Gaia EDR3 (Gaia Collaboration et al. 2021) are also included.

A description of the information for stars in the final sample catalog is presented in Table 3. The final stellar-parameter sample catalog will be released by the SAGES project as a value added catalog. This sample already represents large progress on the development of stellar samples from the Northern sky for use in Galactic studies. Together with our former effort from SMSS DR2 described in the first paper in this series, the sum of which represent photometric metallicities for on the order of 50 million stars, these results will shed light on understanding the formation and evolutionary history of our Galaxy.

The next step of this project is to extend this technique to derive photometric-metallicity with improved precision, especially at the metal-poor end, and other elemental-abundance ratios (e.g.,  $[\alpha/\text{Fe}]$  and [C/Fe]) from the narrow/medium-band photometric surveys (e.g., J/S-PLUS, Cenarro et al. 2019; Mendes de Oliveira et al. 2019), or from Gaia XP low-resolution spectra, although only for stars with a relatively bright limiting magnitude around  $G \sim 17.5$  mag (Gaia Collaboration et al. 2023; Andrae et al. 2023).

## 6. Summary

In this paper, the second paper of this series, we present stellar parameters for over 20 million stars in the Northern sky, using SAGES DR1 and Gaia EDR3. With a careful and comprehensive selection of a training set from spectroscopic measurements, we present photometric-metallicity estimates for nearly 26 million stars (23 million dwarf and 3 million giant stars), with useful metallicity determinations down to [Fe/H] = -3.5. Both internal and external checks show that the precisions of our photometric measurements are about 0.1 dex in the metal-rich range ([Fe/H] > -1.0) and 0.15-0.25/0.3-0.4 dex for dwarf/giant stars with  $[Fe/H] \le -1.0$ . This result is comparable to or even better than obtained for the low/medium-resolution spectroscopy. In addition to metallicity, the final sample also includes measurements of effective temperature from metallicity-dependent  $T_{\rm eff}$ -color relations, distances either from Gaia parallax measurements or from the metallicity-dependent color-absolute magnitude fiducials, and ages from comparisons between observations and stellar isochrones. Radial velocities from spectroscopic surveys and astrometric parameters from Gaia EDR3 are also included.

To date, we have delivered stellar parameters for over 50 million stars covering almost  $3\pi$  steradians of sky, which will be useful to a variety of studies of the Milky Way.

#### Acknowledgments

This work is supported by National Key R&D Program of China No. 2019YFA0405500 and National Natural Science Foundation of China grants 11903027, 11833006, 11973001, 11603002, 11811530289, and U1731108. We used data from the European Space Agency mission Gaia (http://www.cosmos.esa.int/gaia), processed by the Gaia Data Processing and Analysis Consortium (DPAC; see http://www.cosmos.esa.int/web/gaia/dpac/consortium). T.C.B. acknowledges partial support from grant PHY 14-30152, Physics Frontier Center/JINA Center for the Evolution of the Elements (JINA-CEE), awarded by the US National Science Foundation. His participation in this work was initiated by conversations that took place during a visit to China in 2019, supported by a PIFI

Distinguished Scientist award from the Chinese Academy of Science. Y.S.L. acknowledges support from the National Research Foundation (NRF) of Korea grant funded by the Ministry of Science and ICT (NRF-2021R1A2C1008679). Y.S.L. also gratefully acknowledges partial support for his visit to the University of Notre Dame from OISE-1927130: The International Research Network for Nuclear Astrophysics (IReNA), awarded by the US National Science Foundation. C.A.O. acknowledges support from the Australian Research Council through Discovery Project DP190100252.

The national facility capability for SkyMapper has been funded through ARC LIEF grant LE130100104 from the Australian Research Council, awarded to the University of Sydney, the Australian National University, Swinburne University of Technology, the University of Queensland, the University of Western Australia, the University of Melbourne, Curtin University of Technology, Monash University and the Australian Astronomical Observatory. SkyMapper is owned and operated by The Australian National University's Research School of Astronomy and Astrophysics. The survey data were processed and provided by the SkyMapper Team at ANU. The SkyMapper node of the All-Sky Virtual Observatory (ASVO) is hosted at the National Computational Infrastructure (NCI). Development and support the SkyMapper node of the ASVO has been funded in part by Astronomy Australia Limited (AAL) and the Australian Government through the Commonwealth's Education Investment Fund (EIF) and National Collaborative Research Infrastructure Strategy (NCRIS), particularly the National eResearch Collaboration Tools and Resources (NeC-TAR) and the Australian National Data Service Projects (ANDS).

The Guoshoujing Telescope (the Large Sky Area Multi-Object Fiber Spectroscopic Telescope, LAMOST) is a National Major Scientific Project built by the Chinese Academy of Sciences. Funding for the project has been provided by the National Development and Reform Commission. LAMOST is operated and managed by the National Astronomical Observatories, Chinese Academy of Sciences.

## **ORCID iDs**

Yang Huang https://orcid.org/0000-0003-3250-2876 Timothy C. Beers https://orcid.org/0000-0003-4573-6233 Haibo Yuan https://orcid.org/0000-0003-2471-2363 Ke-Feng Tan https://orcid.org/0000-0003-0173-6397 Wei Wang https://orcid.org/0000-0002-9702-4441 Jie Zheng https://orcid.org/0000-0001-6637-6973 Young Sun Lee https://orcid.org/0000-0001-5297-4518 Hai-Ning Li https://orcid.org/0000-0002-0389-9264 Jing-Kun Zhao https://orcid.org/0000-0003-2868-8276 Xiang-Xiang Xue https://orcid.org/0000-0002-0642-5689 Huawei Zhang https://orcid.org/0000-0002-7727-1699 Christian Wolf https://orcid.org/0000-0002-4569-016X Christopher A. Onken https://orcid.org/0000-0003-0017-349X Jifeng Liu https://orcid.org/0000-0002-2874-2706 Zhou Fan https://orcid.org/0000-0002-6790-2397 Gang Zhao https://orcid.org/0000-0002-8980-945X

## References

Abdurro'uf, Accetta, K., Aerts, C., et al. 2022, ApJS, 259, 35 Ahumada, R., Allende Prieto, C., Almeida, A., et al. 2020, ApJS, 249, 3 Andrae, R., Rix, H.-W., & Chandra, V. 2023, ApJS, 267, 8 Aoki, W., Li, H., Matsuno, T., et al. 2022, ApJ, 931, 146 Arentsen, A., Aguado, D. S., Sestito, F., et al. 2023, MNRAS, 519, 5554

```
Bailer-Jones, C. A. L., Rybizki, J., Fouesneau, M., Demleitner, M., &
   Andrae, R. 2021, AJ, 161, 147
Beers, T. C., Preston, G. W., & Shectman, S. A. 1985, AJ, 90, 2089
Beers, T. C., Preston, G. W., & Shectman, S. A. 1992, AJ, 103, 1987
Bessell, M., Bloxham, G., Schmidt, B., et al. 2011, PASP, 123, 789
Bressan, A., Marigo, P., Girardi, L., et al. 2012, MNRAS, 427, 127
Buder, S., Sharma, S., Kos, J., et al. 2021, MNRAS, 506, 150
Cantat-Gaudin, T., Fouesneau, M., Rix, H.-W., et al. 2023, A&A, 669, A55
Casagrande, L., Wolf, C., Mackey, A. D., et al. 2019, MNRAS, 482, 2770
Castro-Ginard, A., Brown, A. G. A., Kostrzewa-Rutkowska, Z., et al. 2023,
Cenarro, A. J., Moles, M., Cristóbal-Hornillos, D., et al. 2019, A&A, 622, A176
Chambers, K. C., Magnier, E. A., Metcalfe, N., et al. 2016, arXiv:1612.05560
Chiti, A., Frebel, A., Mardini, M. K., et al. 2021, ApJS, 254, 31
Christlieb, N. 2003, RvMA, 16, 191
De Silva, G. M., Freeman, K. C., Bland-Hawthorn, J., et al. 2015, MNRAS,
  449, 2604
Deng, L.-C., Newberg, H. J., Liu, C., et al. 2012, RAA, 12, 735
Ezzeddine, R., Rasmussen, K., Frebel, A., et al. 2020, ApJ, 898, 150
Fan, Z., Zhao, G., Wang, W., et al. 2023, ApJS, 268, 9
Green, G. M., Schlafly, E., Zucker, C., Speagle, J. S., & Finkbeiner, D. 2019,
   ApJ, 887, 93
Gaia Collaboration, Montegriffo, P., Bellazzini, M., et al. 2023, A&A, 647, 33
Gaia Collaboration, Brown, A. G. A., Vallenari, A., et al. 2021, A&A, 649, A1
Hansen, T. T., Holmbeck, E. M., Beers, T. C., et al. 2018, ApJ, 858, 92
Holmbeck, E. M., Hansen, T. T., Beers, T. C., et al. 2020, ApJS, 249, 30
Huang, Y., Beers, T. C., Wolf, C., et al. 2022, ApJ, 925, 164
Huang, Y., Chen, B. Q., Yuan, H. B., et al. 2019, ApJS, 243, 7
Huang, Y., Liu, X. W., Chen, B. Q., et al. 2018, AJ, 156, 90
Katz, D., Sartoretti, P., Guerrier, A., et al. 2023, A&A, 674, 5
Kunder, A., Kordopatis, G., Steinmetz, M., et al. 2017, AJ, 153, 75
Lee, Y. S., Beers, T. C., Carlin, J. L., et al. 2015, AJ, 150, 187
Li, H., Aoki, W., Matsuno, T., et al. 2022, ApJ, 931, 147
Liu, X. W., Yuan, H. B., Huo, Z. Y., et al. 2014, in IAU Symp. 298, Setting the
   Scene for Gaia and LAMOST, ed. S. Feltzing et al. (Cambridge: Cambridge
   Univ. Press), 310
```

```
Lucchesi, R., Lardo, C., Jablonka, P., et al. 2022, MNRAS, 511, 1004
Majewski, S. R., Schiavon, R. P., Frinchaboy, P. M., et al. 2017, AJ,
   154, 94
Marigo, P., Girardi, L., Bressan, A., et al. 2017, ApJ, 835, 77
Mendes de Oliveira, C., Ribeiro, T., Schoenell, W., et al. 2019, MNRAS,
Nordström, B., Mayor, M., Andersen, J., et al. 2004, A&A, 418, 989
Norris, J. E., & Yong, D. 2019, ApJ, 879, 37
Onken, C. A., Wolf, C., Bessell, M. S., et al. 2019, PASA, 36, e033
Onken, C. A., Wolf, C., Bian, F., et al. 2022, MNRAS, 511, 572
Riello, M., De Angeli, F., Evans, D. W., et al. 2021, A&A, 649, A3
Rockosi, C. M., Lee, Y. S., Morrison, H. L., et al. 2022, ApJS, 259, 60
Sakari, C. M., Placco, V. M., Farrell, E. M., et al. 2018, ApJ, 868, 110
Sanders, J. L., & Das, P. 2018, MNRAS, 481, 4093
Schlafly, E. F., & Finkbeiner, D. P. 2011, ApJ, 737, 103
Schlegel, D. J., Finkbeiner, D. P., & Davis, M. 1998, ApJ, 500, 525
Shank, D., Komater, D., Beers, T. C., Placco, V. M., & Huang, Y. 2022a,
      IS, 261, 19
Shank, D., Beers, T. C., Placco, V. M., et al. 2022b, ApJ, 926, 26
Soubiran, C., Le Campion, J.-F., Brouillet, N., & Chemin, L. 2016, A&A,
Starkenburg, E., Martin, N., Youakim, K., et al. 2017, MNRAS, 471, 2587
Steinmetz, M., Zwitter, T., Siebert, A., et al. 2006, AJ, 132, 1645
Strömgren, B. 1956, VA, 2, 1336
Suda, T., Katsuta, Y., Yamada, S., et al. 2008, PASJ, 60, 1159
Sun, Y., Yuan, H., & Chen, B. 2022, ApJS, 260, 17
Wolf, C., Onken, C. A., Luvaul, L. C., et al. 2018, PASA, 35, e010
Xue, X.-X., Ma, Z., Rix, H.-W., et al. 2014, ApJ, 784, 170
Yanny, B., Rockosi, C., Newberg, H. J., et al. 2009, AJ, 137, 4377
York, D. G., Adelman, J., Anderson, J. E. J., et al. 2000, AJ, 120, 1579
Yuan, H. B., Liu, X. W., & Xiang, M. S. 2013, MNRAS, 430, 2188
Yuan, Z., Malhan, K., Sestito, F., et al. 2022, ApJ, 930, 103
Zepeda, J., Rasmussen, K. C., Beers, T. C., et al. 2022, ApJ, 927, 13
Zhang, R., & Yuan, H. 2023, ApJS, 264, 14
Zheng, J., Zhao, G., Wang, W., et al. 2018, RAA, 18, 147
Zhou, X., Fan, X.-H., Fan, Z., et al. 2016, RAA, 16, 69
```